Available online at www.sciencedirect.com
ScienceDirect
Journal of Power Sources 169 (2007) 71–76
JOURNAL OF POWER SOURCES
www.elsevier.com/locate/jpowsour

Short communication

Bifunctional amorphous alloys more tolerant to carbon monoxide☆

J. Barranco, A.R. Pierna*

Chemical Engineering and Environment Department, University of the Basque Country, Plaza de Europa 1, 20018 San Sebastián, Spain

Available online 16 February 2007

Abstract

The aim of this work is the study of the electrochemical behaviour of methanol and CO electro-oxidation reaction with amorphous metallic alloys of compositions $(NiNb)_{99}(PtX)_1$ (X = Ru, Sn, compositions in at.%), which are obtained by mechanical alloying, that results to in powders used as modified carbon paste electrodes (MCPEs).

The presence of tin drastically decreases the reactivity towards methanol electro-oxidation of the alloy, followed by the $Ni_{59}Nb_{40}Pt_1$ and $Ni_{59}Nb_{40}Pt_{0.6}Ru_{0.4}$ alloys. Differential electrochemical mass spectrometry (DEMS) studies demonstrate that the $Ni_{59}Nb_{40}Pt_{0.6}Ru_{0.4}$ and $Ni_{59}Nb_{40}Pt_{0.6}Sn_{0.4}$ electrodes show the best tolerance to CO produced by methanol deprotonation, giving rise to more negative onset potential values for the CO_2 production, although the voltammograms for the stripping of a CO monolayer clearly show that the electrode that possesses a better tolerance to CO adsorbed on the surface of the electrode is $Ni_{59}Nb_{40}Pt_{0.6}Sn_{0.4}$, decreasing the onset potential values 281 and 158 mV with regard to the $Ni_{59}Nb_{40}Pt_1$ and $Ni_{59}Nb_{40}Pt_{0.6}Ru_{0.4}$, respectively. The catalytic activity of the electrode formed might be attributed to an adsorbed state of CO unique in this alloy.

Keywords: Amorphous alloys; Modified carbon paste electrodes; Electrocatalysis; Fuel cells

1. Introduction

Vehicles powered by fuel cells are currently considered by the automotive industry as a realistic alternative to the internal combustion engine. The search for alternative propulsion systems is experiencing an excellent and extensive development concerning health issues, global warning and oil reserves during the last decade.

Nowadays, some types of fuel cells are approaching commercialization. The most expected types are direct methanol fuel cells (DMFC) and polymer electrolyte membrane fuel cells (PEMFC). Unlike other types of fuel cells, DMFC need no fuel processor to reform hydrocarbon fuels. This fact makes DMFC advantageous to be applied to small and portable devices. But the intrinsic low power density of such fuel cells is a problem that must be overcome.

Catalysis by amorphous materials is no more an incipient area of research. Although some amorphous materials have been found to be useful in industrial catalysis, the rapid progress that is being made in the preparation and stabilization of new materials has opened new possibilities for developing new catalysts, which works as anodes for DMFC.

These amorphous materials are expected to have a high concentration of low coordinate active sites at their surfaces [1,2]. They are single phase, and the concentration gradients should be minimal so they offer the advantage, compared with other materials, minimizing the catalytically important phenomena such as surface segregation. Above all of these characteristics, the lack of a specific orientation of the metals used as electrocatalytically active sites is of great importance because of the behaviour of such electrodes towards a defined process (i.e. methanol, CO or ethanol, ..., electro-oxidation), contrary to what has been inferred in many works regarding the surface orientation dependence of methanol electro-oxidation processes, on Pt, Au single crystal electrodes and Pt polycrystalline based alloys [3–5].

Relatively much electrochemical work has been carried out on metal–metal glasses, but not many have been focused on the polyphasic crystalline (Ni–Nb)-based alloys [6,7]. The composition $Ni_{60}Nb_{40}$ is very similar one of the eutectic compositions in the Ni–Nb phase diagram, so glasses of this composition are readily formed. Ni_{60}–Nb_{40} polyphasic alloys have been recently used as a matrix in new amorphous alloys [8]. These have been alloyed with $Pt_{(1-x)}$ Y_x (Y = Ru, Sn, $x = 1$, 0.6 at.%) metals, and further used as catalyst components for anode materials for

☆ This paper presented at the 2nd National Congress on Fuel Cells, CONAPPICE 2006.

* Corresponding author. Tel.: +34 943 017183; fax: +34 943 017130.
E-mail address: iapropia@sp.ehu.es (A.R. Pierna).

0378-7753/$ – see front matter © 2007 Elsevier B.V. All rights reserved.
doi:10.1016/j.jpowsour.2007.02.006

the electrochemical treatment of toxic compounds, and for its application in fuel cells [9,10].

In the present paper, the effects of adding tin and ruthenium in the platinum $Ni_{60}Nb_{40}$-based alloys on adsorbed CO_{ads} and methanol oxidation reactions are studied by different electrochemical and in situ (DEMS) techniques.

2. Experimental

2.1. Electrode and solutions

Preparation of the catalytic powders (CPs) was achieved by the mechanical alloying technique. Ni (Goodfellow 250 μm powder), Pt (Goodfellow, 45 μm powder), Sn (Goodfellow, 45 μm powder) and Ru (Acrós Organics −200 mesh powder) were introduced in a Retsch PM 400 planetary ball mill during 40 h using a stainless steel vial and balls with a ball to powder ratio of 4:1. Their chemical composition, in at.%, was tested by inductively coupled plasma (ICP) technique.

Carbon paste electrodes were made by hand-mixing the CPs with glassy carbon powder (Aldrich, 2–12 μm) and paraffin, as the binder (Uvasol® from Merck). All of the three alloys have been chemically activated by immersion an analytical grade HF 48% solution for 30 s at room temperature, and subsequently rinsed out with double-distilled water. After that, and before any electrochemical measurement, the repetitivity of catalytic response was tested by cycling such electrodes several times during a cyclic voltammetry experience in 1 M $HClO_4$ as supporting electrolyte, until a repetitive voltammogram was achieved.

2.2. Experimental setup

The electrochemical setup consists of one cell, and a flow-cell procedure that has been used to allow the change of electrolyte solutions under potential control and in an air free atmosphere. A three-electrode system and a multipotenciostat (Solartron 1480 multistat system), driven by a Corrware® Software program, were used for all cyclic voltammetries (CVs). The working electrodes had a geometric area of 0.28 cm^2, and the counter electrode used was a high area glassy carbon electrode. A commercial Ag/AgCl (KCl 3 M, Crisolyt A) electrode was used as the reference electrode, although all potentials in this paper are quoted vs. the normal hydrogen electrode (NHE).

For DEMS experiments, an electrochemical plexiglass cell (2 cm^3 capacity) was connected to the chamber containing the quadruple mass spectrometer (MS) with a Channeltron detector BALZER QMG 112. The interface between the cell and the vacuum consisted of a porous teflon membrane (Scimat, 60 μm thick, 0.2 pore diameter, 50% porosity). A conventional three electrode arrangement was employed for the electrochemical measurements. A normal hydrogen electrode (NHE) was prepared in the supporting electrolyte (0.1 M $HClO_4$) and a platinum wire used as the counter-electrode. Mass spectrometry cyclic voltammograms (MSCVs) for selected mass to charge (*m*/*z*) ratios were recorded simultaneously with the cyclic voltammograms (CVs) using as working electrodes those described in the previous section.

3. Results and discussion

3.1. Physical characterization of the electrodes

The amorphous nature and evolution of structure of the powders were confirmed by X-ray diffraction (XRD) and differential scanning calorimetry (DSC). Fig. 1a shows the thermogram at 0 h and 40 h of the DSC experiment for the $Ni_{59}Nb_{40}Pt_{0.6}Sn_{0.4}$ MCPE obtained from 200 °C up to 700 °C at a heating rate of 10 °C min^{-1} in N_2 atmosphere. As it can be observed, the thermogram for the non-alloyed sample shows several peaks typically assigned to crystalline structures at 232 and 359 °C, corresponding to the melting point and to the curie temperature of tin, respectively. Such peaks disappear when the sample is alloyed and an amorphous structure is obtained, as it can be seen in the thermogram at 40 h. In relation to the amorphous

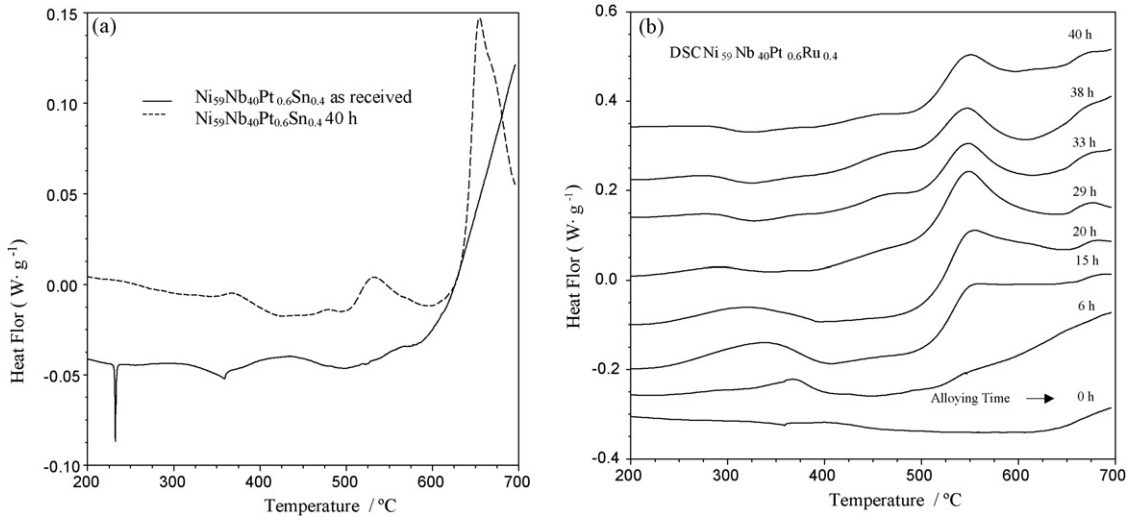

Fig. 1. DSC traces for the $Ni_{59}Nb_{40}Pt_{0.6}Sn_{0.4}$ powders as-received and after 40 h milling time (a) and DSC traces of the $Ni_{59}Nb_{40}Pt_{0.6}Ru_{0.4}$ powders at different milling times (b), obtained at a constant heating rate of 10 °C min^{-1} in N_2 atmosphere.

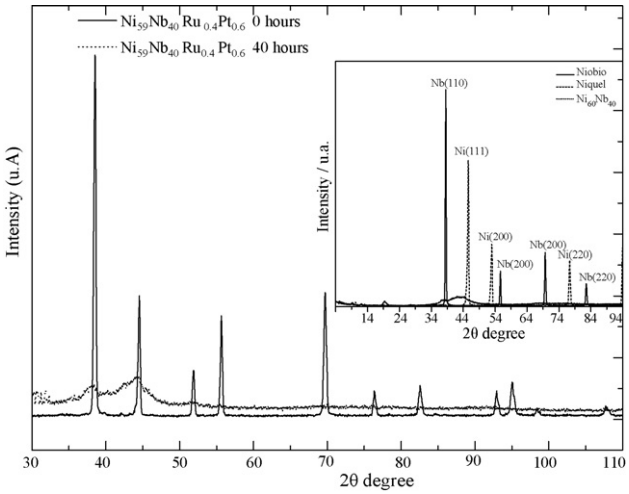

Fig. 2. XRD traces from $Ni_{59}Nb_{40}Pt_{0.6}Ru_{0.4}$ powders as-received and after 40 h milling time. Insert: XRD from Ni, Nb as-received powders and $Ni_{60}Nb_{40}$ 40 h allowed powders.

phases, two wide peaks can be observed at 532 and 652 °C which can be assigned to Ni_3Nb phase structure and the NiNb μ-phase structure, i.e., the equilibrium phases, respectively. At this composition the crystallized products of the present work are the same as those of Koch et al. and Lee et al. [11,12]. Fig. 1b shows DSC traces from the $Ni_{59}Nb_{40}Pt_{0.6}Ru_{0.4}$ powder as-received (0 h) and after different milling times. For milling times shorter than 11 h, the DSC traces showed three broad exothermic peaks around 290, 380 and 560 °C which are caused by annihilation of lattice defects at 290 °C, the formation of an amorphous phase between Ni–Sn and Nb layers at 380 °C and its subsequent crystallization at 560 °C. With increasing milling time, one further exothermic peak at 652 °C, appeared on the DSC traces which merged at 21 h of milling time and attributed to the already mentioned NiNb μ-phase structure [12].

Fig. 2 shows XRD traces from $Ni_{59}Nb_{40}Pt_{0.6}Ru_{0.4}$ powders as-received and after 40 h milling time. It can be observed how the sharp crystalline diffraction peaks of the as-received powder broadened, showing an amorphous peak center at 40°. The insert shows the $Ni_{60}Nb_{40}$ XRD traces as-received and after 40 h of milling time showing the disappearance of the different sharp peaks as the amorphous peak appears.

3.2. Methanol electro-oxidation

The cyclic voltammogram (CV) of the $Ni_{59}Nb_{40}Pt_1$ electrode in 1 M $HClO_4$ at $dE/dt = 50\,mV\,s^{-1}$ is shown in Fig. 3a. The shape of such voltammogram resembles those of the polycrystalline Pt [13,14] with three well distinguished anodic zones, i.e. hydrogen evolution zone from 0 to 355 mV, double layer zone from 442 to 598 mV, Pt oxidation zone from 598 mV up to 1300 mV. Above 1400 mV oxygen evolution begins. During the cathodic scan, a Pt–O reduction broad peak appears at 545 mV. The CV of the $Ni_{59}Nb_{40}Pt_{0.6}Ru_{0.4}$ and $Ni_{59}Nb_{40}Pt_{0.6}Sn_{0.4}$ is shown in Fig. 3b and c, respectively. As it can be observed, the peak related to the different areas of formation and reduction of Pt oxides disappears. This absence of peak of oxidation and

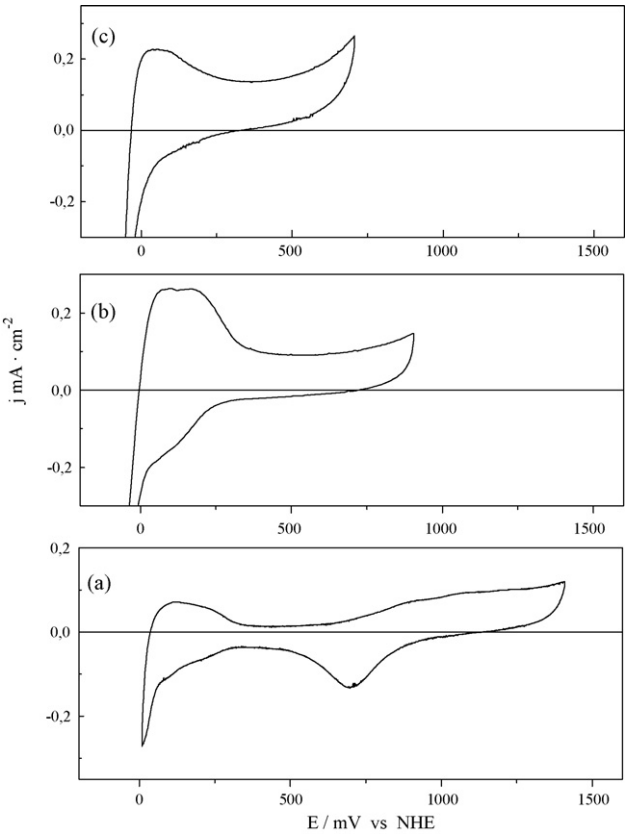

Fig. 3. Cyclic voltammograms of $Ni_{59}Nb_{40}Pt_1$ (a), $Ni_{59}Nb_{40}Pt_{0.6}Ru_{0.4}$ (b) and $Ni_{59}Nb_{40}Pt_{0.6}Sn_{0.4}$ (c) MCPEs in 1 M $HClO_4$ at 50 mV s^{-1}, and 25 °C.

reduction of the Pt–O_{ads} is owed to the easiness with which binary mixtures eliminate the sludge of Pt–O formed on the surface of the electrodes, also observed by Aricó et al. [15], and the fact that Ru(II) oxide/hydroxide, as well as Sn oxides are masked in the hydrogen/double layer range of potentials [16]. Voltammetries of the different electrodes in 1 M $HClO_4$, have been used to measure the real surface area, taking into account the accepted normalization factor of 210 μC cm^{-2} as a measure of nearly a monolayer of adsorbed hydrogen on polycrystalline platinum.

Table 1 shows values of the onset potential (E_{onset}), peak potential (E_p), maximum current density (j_p), real surface area (S_r), rugosity and mass activity of amorphous $Ni_{59}Nb_{40}Pt_1$, $Ni_{59}Nb_{40}Pt_{0.6}Ru_{0.4}$ and $Ni_{59}Nb_{40}Pt_{0.6}Sn_{0.4}$ MCPEs and Pt polycrystalline electrodes. The values of current densities are normalized to the real surface area obtained by the method already mentioned. As it can be observed, the major current density values are obtained for the $Ni_{59}Nb_{40}Pt_{0.6}Ru_{0.4}$ electrode, followed by $Ni_{59}Nb_{40}Pt_1$ and $Ni_{59}Nb_{40}Pt_{0.6}Sn_{0.4}$ electrodes. It is well known that adding a co-catalyst to Pt enhances the reactivity of such alloys toward the methanol deprotonation process, following the so-call bifunctional mechanism [17]. Apparently, this must not be the only reason for such behaviour. $Ni_{59}Nb_{40}Pt_{0.6}Sn_{0.4}$ electrode voltammogram shows a negative shift of maximum peak potential of ca. 0.1 V showing an enhancement in methanol deprotonation, although j_p values are, in comparison, very low. So alloying the Pt with different

Table 1
Onset potential E_{onset}, current density (j_p), peak potential (E_p), real surface area (S_r), and mass activity (MA) of $Ni_{59}Nb_{40}Pt_1$, $Ni_{59}Nb_{40}Pt_{0.6}Sn_{0.4}$, $Ni_{59}Nb_{40}Pt_{0.6}Ru_{0.4}$ MCPEs, and $Pt_{polycrystalline}$

Alloys	E_{onset} (V)	E_p (V)	j_p ($\mu A\,cm^{-2}$)	S_r (cm^2)	Rugosity	MA[a] ($A\,g^{-1}$)
$Ni_{59}Nb_{40}Pt_1$	0.50	1.1	581	4.6	16	6.4
$Ni_{59}Nb_{40}Pt_{0.6}Sn_{0.4}$	0.47	1.0	454	3.2	11	3.1
$Ni_{59}Nb_{40}Pt_{0.6}Ru_{0.4}$	0.43	0.88	1571	3.3	12	6.5
$Pt_{policristlino}$ (layer)	0.62	1.15	530	2.9	1.45	8.9

1.56 M MeOH, 1 M $HClO_4$, 50 mV s^{-1}, 25 °C.
[a] MA ($A\,g^{-1}$) = (j_p/m_d) × 10^3.

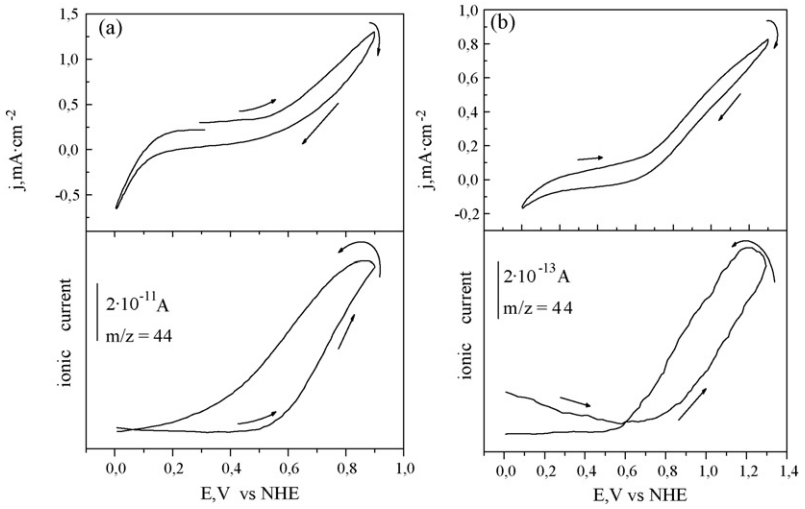

Fig. 4. 0.1 M CH_3OH oxidation in 0.1 M $HClO_4$, and CO_2 ($m/z = 44$, $[CO_2]^+$) production for (a) $Ni_{59}Nb_{40}Pt_{0.6}Ru_{0.4}$ and (b) $Ni_{59}Nb_{40}Pt_{0.6}Sn_{0.4}$ MCPEs. Geometric area 0.28 cm^2, 25 °C.

co-catalyst may modify the Pt electronic structure and weaken the Pt-MeOH deprotonation due to the less free active centres of Pt, as predicted by the ligand model [18–22]. The CVs and simultaneously recorded MSCVs related to the production of CO_2 ($m/z = 44$) during the methanol deprotonation for $Ni_{59}Nb_{40}Pt_{0.6}Ru_{0.4}$ and $Ni_{59}Nb_{40}Pt_{0.6}Sn_{0.4}$ containing MCPEs, Fig. 4 show the peak potential shift to more positive potentials for the Sn-containing electrode. Thus the presence of Sn does not seem to enhance the methanol deprotonation. From this, we can infer that the decrease of the faradic current in CV is mainly related to the diminution in the signal $m/z = 44$, i.e. the reaction pathway involving the production of CO_2 through CH_3OH deprotonation, which is mainly related to the adsorbed species at the electrode, is not favourable.

Tafel plots, Fig. 5 obtained at 50 mV s^{-1} for $Ni_{59}Nb_{40}Pt_1$, $Ni_{59}Nb_{40}Pt_{0.6}Sn_{0.4}$, $Ni_{59}Nb_{40}Pt_{0.6}Ru_{0.4}$ electrodes, ca. 204, 308 and 145 mV dec^{-1}, respectively, enable us to obtain symmetry coefficients for each electrode, and kinetic parameters for methanol electro-oxidation. Values of symmetry coefficients (α), as well as diffusion coefficients D ($cm^2\,s^{-1}$) and number of electrons of the limiting reaction (n_a) are shown in Table 2. As it can be observed, symmetry coefficient values of these MCPEs are close to unity, which is characteristic for an irreversible process. Taken this fact into account, the rest of the kinetic parameters were calculated using the current density versus D relation for an irreversible process as well as the peak

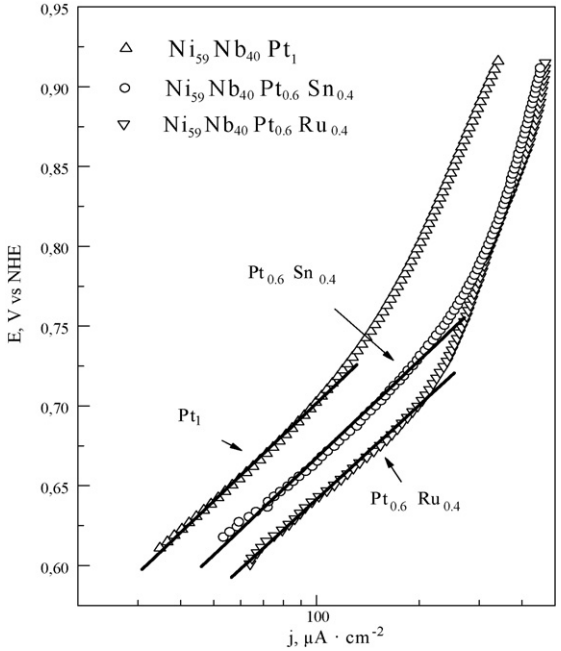

Fig. 5. Tafel plots for $Ni_{59}Nb_{40}Pt_1$, $Ni_{59}Nb_{40}Pt_{0.6}Sn_{0.4}$ and $Ni_{59}Nb_{40}Pt_{0.6}Ru_{0.4}$ MCPEs 1 M $HClO_4$ 1.56 M CH_3OH, 50 mV s^{-1}, 25 °C. Normalized with the real surface area (S_r) of Pt (obtained by CO stripping method).

Table 2
Symmetry coefficients (α), diffusion coefficients D ($cm^2\ s^{-1}$) and number of electrons of the limiting reaction (n_a) values

Alloy	α	dE/d(log v) (mV)	αn_a	B, $2.99 \times 10^5 n v^{1/2} D^{1/2} (\alpha n_a)^{1/2}$	D ($cm^2\ s^{-1}$)
$Ni_{59}Nb_{40}Pt_1$	0.95	0.066	0.6	242	6.0×10^{-7}
$Ni_{59}Nb_{40}Pt_{0.6}Sn_{0.4}$	0.97	0.043	0.7	216	4.1×10^{-6}
$Ni_{59}Nb_{40}Pt_{0.6}Ru_{0.4}$	0.94	0.047	0.5	1044	1.4×10^{-6}

potential and half peak potential difference

$$j_p = 2.99 \times 10^5 n(\alpha n_a)^{1/2} C D^{1/2} v^{1/2},$$

$$E_p - E_{p/2}\,(\text{mV}) = \frac{47.7}{\alpha n_a}, \qquad E_p - E_{p/2}\,(\text{mV}) = \frac{47.7}{\alpha n_a}$$

where v is the scan rate of the experiment in $mV\ s^{-1}$.

3.3. CO electro-oxidation

The comparison of catalyst activities for CO selective oxidation is displayed in Fig. 6 as stripping voltammograms of saturated CO adlayer adsorbed at 0.043 V on $Ni_{59}Nb_{40}Pt_1$, $Ni_{59}Nb_{40}Pt_{0.6}Sn_{0.4}$ and $Ni_{59}Nb_{40}Pt_{0.6}Ru_{0.4}$ amorphous MCPEs surfaces. Basic cyclic voltammograms in clean electrolyte media of CO are also shown. $Ni_{59}Nb_{40}Pt_{0.6}Sn_{0.4}$ as well as $Ni_{59}Nb_{40}Pt_{0.6}Ru_{0.4}$ amorphous electrodes clearly show a better tolerance to CO adsorbed on the surface of the electrode, decreasing the onset potential values 281 and 134 mV with respect to the $Ni_{59}Nb_{40}Pt_1$. The negative shift

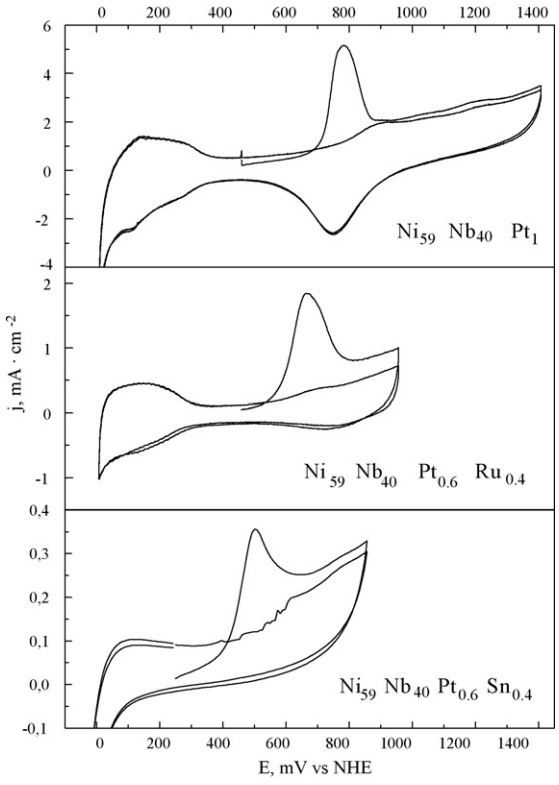

Fig. 6. CO striping for MCPEs: $Ni_{59}Nb_{40}Pt_1$, $Ni_{59}Nb_{40}Pt_{0.6}Sn_{0.4}$, $Ni_{59}Nb_{40}Pt_{0.6}Ru_{0.4}$. 1 M $HClO_4$, 0.043 V adsorption potential, 50 mV s^{-1}, 25 °C. Geometric area 0.28 cm^{-2}.

in CVs at the beginning of the oxidation of adsorbed CO on $Ni_{59}Nb_{40}Pt_{0.6}Ru_{0.4}$ and $Ni_{59}Nb_{40}Pt_{0.6}Sn_{0.4}$ amorphous electrodes, compared with $Ni_{59}Nb_{40}Pt_1$ alloy, is in agreement with Jiang et al. and Vigier et al. [23,24]. The Langmmuir–Hinshelwood mechanism for oxidative removal of adsorbed CO with chemisorbed oxygen, has often been invoked to explain the oxidation of CO adsorbed on Pt surfaces in an electrolyte [25,26]. According to the bifunctional mechanism [27], the electrochemical oxidation of CO_{ads} on the bicatalytic alloys $Ni_{59}Nb_{40}Pt_{0.6}Ru_{0.4}$ and $Ni_{59}Nb_{40}Pt_{0.6}Sn_{0.4}$ surfaces, occurs in two major steps: (1) water dissociates on free Ru or Sn sites giving adsorbed OH, which then can initiate further electro-oxidation (2) of CO molecules adsorbed on Pt or Ru or Sn neighbouring sites, following a bimolecular reaction between oxygen-containing species OH_{ads} and adsorbed CO. These steps can be summarized as follows:

$$Pt + CO_{diss} \rightarrow Pt - CO_{ads},$$

$$M + H_2O \rightarrow M - OH_{ads} + H^+ + e^- \quad (M = Ru, Sn),$$

$$Pt - CO_{ads} + M - OH_{ads} \rightarrow Pt + M + CO_2 + H^+ + e^-$$

The presence of Sn or Ru in the alloy allows for the continuous oxidation of the CO at a potential where OH_{ads} does not form on Pt.

This bifunctional mechanism explains the shift to more negative values of the onset potentials of the alloys containing Sn or Ru, although the explanation of the even more negative shift of the onset and potential peak for the CO oxidation of the $Ni_{59}Nb_{40}Pt_{0.6}Sn_{0.4}$ electrode expected for further results of in situ FTIR spectra during CO oxidation on the surfaces of the different electrodes, can be inferred from the existence of either a major CO bridge (CO_B) bonding, which are said to have a low value of adsorption energy in the saturated adlayer, or according to Gasteiger et al. [28], the high catalytic activity of $Ni_{59}Nb_{40}Pt_{0.6}Sn_{0.4}$ electrode can be attributed to an adsorbed state of CO unique in this alloy.

4. Conclusions

From the catalytic activity of the amorphous electrodes and in particular, comparing different structural nature of the two Pt-containing electrodes, amorphous and crystalline, we can infer that the different structures show different behaviors towards the methanol electro-oxidation. As can be seen in Table 1, the onset potential of methanol electro-oxidation on the amorphous $Ni_{59}Nb_{40}Pt_1$ MCPE, shifts 120 mV towards negative potential values, with respect of Pt polycrystalline. The catalytic activity is enhanced also for these $Ni_{59}Nb_{40}Pt_1$ alloys with respect of Pt polycrystalline, even with the presence in its composition of only

1 at.% in Pt. Also the addition of a co-catalyst seems to favor the onset potential of such reaction shifting the onset potential 150 and 190 mV towards negative values of potential. The activity of the latest is enhanced only with an amount of 0.4 at.% in Pt in their compositions.

From DEMS technique we can infer that the decrease of the faradic current in CV is mainly related to de diminution in the signal $m/z = 44$, i.e. the reaction pathway involving the production of CO_2 through CH_3OH electro-oxidation, which is mainly related to the adsorbed species at the electrode, is not favourable. This might explain the different behaviour of the Sn containing electrode towards the methanol and CO electro-oxidation processes.

The most important contribution in the CO electro-oxidation concerns the role of tin and ruthenium in the catalysts. These co-catalysts are able to adsorb water molecules, dissociate them to form OH adsorbed species and thus, allowing the formation of CO_2 at lower potentials, although the ligand effect for different alloys seems to have an important role.

Acknowledgments

The authors gratefully acknowledge the technical support in DEMs analysis to E. Pastor and J.M. Rodriguez of the University of La Laguna (ULL), the financial support of the Excelentísima Diputación Foral de Guipúzcoa (project. 206/2005, FEDER), and Basque Govermment (Saoitek 2004-2005 project S-PE04UN26).

References

[1] K.S. Suslick, S.B. Choe, A.A. Cichoulus, M.W. Grinstaff, Nature 353 (1991) 414.
[2] V. Kesavan, D. Dhar, Y. Koltypin, N. Perkas, O. Palchik, A. Gedanken, S. Chandrasekaran, Pure Appl. Chem. 73 (1) (2001) 85–91.
[3] A. Ivic, M. Jovanovic, V. Vlajnic, G. Popic, J. Electroanal. Chem. 423 (1–2) (1997) 119–124.
[4] T. Iwasita, Electrochim. Acta 47 (2002) 3663–3674.
[5] E. Casado-Rivera, D.J. Volpe, L. Alden, C. Lind, C. Downie, T. Vázquez-Alvarez, A.C.D. Angelo, F.J. DoSalvo, H.D. Abruña, J. Am. Chem. Soc. 126 (2004) 4043–4049.
[6] T. Rathz, M.B. Robinson, R.W. Hyers, J.R. Rogers, Proceedings of the 40th Aerospace Science Meeting Exhibition, Reno, NV, January 14–17, 2002.
[7] B. Fang, C. Zhou, X. Liu, S. Duan, J. Appl. Electrochem. 31 (2001) 201–205.
[8] M. Sistiaga, A. Cuesta, A.R. Pierna, C. Gutierrez, Surf. Sci. 410 (1998) 312–320.
[9] M. Sistiaga, A.R. Pierna, J. Non-Crystall. Solids 329 (2003) 184–187.
[10] A.R. Pierna, M. Sistiaga, C. Navascués, A. Lorenzo, J. Non-Crystall. Solids 287 (2001) 432–436.
[11] C.C. Koc, O.B. Cavin, C.G. Mckamey, J.O. Scarbrough, Appl. Phys. Lett. 43 (1983) 11.
[12] P.Y. Lee, C.C. Koch, J. Non-Crystall. Solids 94 (1987) 88–100.
[13] A.R. Pierna, M. Sistiaga, C. Navascués, A. Lorenzo, J. Non-Crystall. Solids 287 (2001) 432–436.
[14] A. Sunita Rani, L.D. Jayaraman, G. Sharma, T.S.R. Murali Dhar, Prasada Rao, J. Electroanal. Chem. 495 (2000) 62–70.
[15] A.S. Aricó, V. Antonucci, N. Giordano, A.K. Shukla, M.K. Ravikumar, A. Roy, S.R. Barman, D.D. Sarma, J. Power sources 50 (1994) 295–309.
[16] Ermete Antolini, Mater. Chem. Phys. 78 (2003) 563–573.
[17] S.Lj. Gojkovic, T.R. Vidakovic, D.R. Durovic, Electrochim. Acta 48 (2003) 3607–3614.
[18] E. Ticianelli, J.G. Beery, M.T. Paffett, S. Gotessfeld, J. Eletroanal. Chem. 258 (1989) 61.
[19] P.A. Christensen, A. Hamnett, G.L. Troughton, J. Electroanal. Chem. 362 (1993) 207.
[20] T. Frelink, W. Visscher, J.A.R. van Veen, Surf Sci. 335 (1995) 353.
[21] P. Waszczuk, G.Q. Lu, A. Wieckowski, C. Lu, C. Rise, R.I. Masel, Electrochim. Acta 47 (2002) 3637.
[22] T. Iwasita, Electrochim. Acta 47 (2002) 3663.
[23] J. Jiang, A. Kucernak, J. Electroanal. Chem. 543 (2003) 187–199.
[24] F. Vigier, C. Coutanceau, F. Hahn, E.M. Belgsir, C. Lamy, J. Electroanal. Chem. 563 (1) (2004) 81–89.
[25] S.C. Chang, L.W.H. Leung, M.J. Weaver, J. Phys. Chem. 94 (1990) 6013.
[26] M.T.M. Koper, T.J. Schmidt, N.M. Markovic, P.N. Ross, J. Phys. Chem. 105 (2001) 8381.
[27] H.A. Gasteiger, N. Markovic, P.N. Ross, E.J. Cairns, J. Phys. Chem. 98 (1994) 617.
[28] H.A. Gasteiger, N. Markovic, P.N. Ross, E.J. Cairns, J. Phys. Chem. 98 (1993) 12020.